

# Surface Defects Reinforced Polymer-Ceramic Interfacial Anchoring for High-Rate Flexible Solid-State Batteries

Yanda Fu, Kai Yang, Shida Xue, Weihan Li, Shiming Chen, Yongli Song, Zhibo Song, Wenguang Zhao, Yunlong Zhao, Feng Pan, Luyi Yang,\* and Xueliang Sun\*

High Li<sup>+</sup> conductivity, good interfacial compatibility and high mechanical strength are desirable for practical utilization of all-solid-state electrolytes. In this study, by introducing Li<sub>6.4</sub>La<sub>3</sub>Zr<sub>1.4</sub>Ta<sub>0.6</sub>O<sub>12</sub> (LLZTO) with surface defects into poly(ethylene oxide) (PEO), a composite solid electrolyte (OV-LLZTO/PEO) is prepared. The surface defects serve as anchoring points for oxygen atoms of PEO chains, forming a firmly bonded polymer-ceramic interface. This bonding effect effectively prevents the agglomeration of LLZTO particles and crystallization of PEO domains, forming a homogeneous electrolyte membrane exhibiting high mechanical strength, reduced interfacial resistance with electrodes as well as improved Li<sup>+</sup> conductivity. Owing to these favorable properties, OV-LLZTO/PEO can be operated under a high current density (0.7 mA cm<sup>-2</sup>) in a Li–Li symmetric cell without short circuit. Above all, solid-state full-cells employing OV-LLZTO/PEO deliver state-of-the-art rate capability (8 C), power density and capacity retention. As a final proof of concept study, flexible pouch cells are assembled and tested, exhibiting high cycle stability under 5 C and excellent safety feature under abusive working conditions. Through manipulating the interfacial interactions between polymer and inorganic electrolytes, this study points out a new direction to optimizing the performance of all-solid-state batteries.

## 1. Introduction

All-solid-state batteries (ASSBs) employing solid electrolytes show great potential to replace commercial Li-ion batteries owing to higher energy density and lower risk of flammability.<sup>[1–3]</sup> Despite the reported progress that have been achieved

for all-solid-state batteries, there are still many challenges for the large-scale commercialization of ASSBs, such as low ionic conductivity,<sup>[4]</sup> unstable interfaces<sup>[1,5–7]</sup> and lithium dendrite related safety issues.<sup>[8]</sup> Polymer solid electrolytes (SPEs) are considered as promising candidates in ASSBs owing to their flexibility and interfacial compatibility.<sup>[9,10]</sup> In principle, high Li<sup>+</sup> conductivity, good interfacial compatibility and robust mechanical strength are crucial parameters for practical utilization of SPEs in ASSBs.<sup>[2,4,7]</sup> However, currently reported SPEs are unable to fit all requirements above. For instance, as a representative SPE, poly(ethylene oxide) (PEO) generally possesses crystalline phase resulting in low ionic conductivity at room temperature.<sup>[11–13]</sup> Moreover, Li<sup>+</sup> is trapped in ether linkage of PEO or anion in electrolyte resulting in low Li<sup>+</sup> transference number ( $t_{Li^+}$ ).<sup>[2,14–16]</sup> Despite exhibiting good interfacial compatibility with Li metal anode, the relatively weak mechanical properties of PEO have posed great

concerns regarding to volume changes during cycling, ability to limit lithium dendrite growth and operational reliability for scalable cell manufacturing.<sup>[12,17,18]</sup>

To address these issues, inorganic/organic composite solid electrolytes (CSEs) have been extensively investigated. On the one hand, the inorganic fillers promote the lithium diffusion by disrupting the crystalline domain of PEO, dissociating anions and Li<sup>+</sup> through Lewis acid-base interaction.<sup>[2,19]</sup> On the other hand, the inorganic fillers within the SPE serve as mechanical buffer to dissipate the stress and limit the lithium dendrite growth.<sup>[20–22]</sup> During the recent decade, inorganic solid electrolytes (ISEs) such as LLZO,<sup>[22–24]</sup> LATP,<sup>[25,26]</sup> LGPS,<sup>[27,28]</sup> etc. have been extensively employed as active fillers to further provide extra lithium diffusion path within SPEs and stabilize the electrolyte/electrode interface. Ideally, a well-designed CSE should inherit the mechanical strength, high ionic conductivity of ISEs and the processability, flexibility of SPEs.<sup>[29]</sup> However, for conventional “ceramic-in-polymer” CSEs, it remains a great challenge to obtain robust mechanical strength while keeping high ionic conductivity.<sup>[22,30]</sup>

While many current studies focus on the macroscopic and bulk properties of CSEs, the interfacial interaction between inorganic particle and polymer electrolyte has a huge impact on

Y. Fu, S. Xue, S. Chen, Y. Song, Z. Song, W. Zhao, F. Pan, L. Yang  
School of Advanced Materials  
Peking University Shenzhen Graduate School  
Shenzhen 518055, China  
E-mail: yangly@pkusz.edu.cn

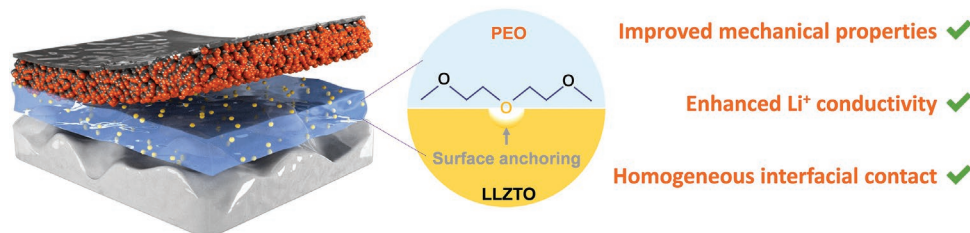
K. Yang, Y. Zhao  
Advanced Technology Institute  
University of Surrey  
Guildford, Surrey GU2 7XH, UK

W. Li, X. Sun  
Department of Mechanical and Materials Engineering  
University of Western Ontario London  
ON N6A 5B9, Canada  
E-mail: xsun9@uwo.ca

 The ORCID identification number(s) for the author(s) of this article can be found under <https://doi.org/10.1002/adfm.202210845>.

DOI: 10.1002/adfm.202210845

### High-rate flexible solid-state battery



**Scheme 1.** Proposed working mechanisms for OV-LLZTO/PEO in an all-solid-state battery.

the overall electrochemical and mechanical properties. Nevertheless, such interface is a confined region of little presence, its properties are usually obscured by the bulk. In this work, oxygen vacancies are introduced into  $\text{Li}_{6.4}\text{La}_3\text{Zr}_{1.4}\text{Ta}_{0.6}\text{O}_{12}$  (LLZTO) to form OV-LLZTO, which is further employed to prepare a PEO-based CSE (OV-LLZTO/PEO). It is revealed oxygen vacancies serve as “anchoring points” for oxygen-containing polymer segments, forming strong binding sites via “shared” O atoms (**Scheme 1**). Consequently, enhanced mechanical strength, reduced interfacial resistance with electrodes and improved  $\text{Li}^+$  conductivity can be achieved. All-solid-state  $\text{LiFePO}_4\|\text{OV-LLZTO/PEO}\|\text{Li}$  cells deliver the highest power density and cycle stability to our best knowledge, which can be attributed to the boosted bulk/interfacial charge transfer. Additionally, benefiting from the enhanced mechanical strength, proof-of-concept flexible pouch cells are assembled and operated under extreme working conditions. Through interfacial molecular regulation, this work defines a new strategy to realize the practical application of composite solid electrolytes.

## 2. Results and Discussion

### 2.1. Improved Properties of OV-LLZTO/PEO

Oxygen vacancies are created in nano-sized LLZTO particles by thermal treatment at 450 °C under reducing atmosphere. The size of LLZTO nanoparticles is about 200 to 500 nm (Figures S1 and S2, Supporting Information), which shows no obvious morphology change and particle agglomeration after thermal treatment. X-ray photoelectron spectroscopy (XPS) is employed to reveal the elemental valence state on the surface of OV-LLZTO particles. Both La 3d (**Figure 1a**) and Zr 3d (**Figure 1b**) spectra show peak shifts toward lower binding energy after thermal treatment, whereas Ta 3d and O 1s spectra show no obvious shifts (**Figure S3**, Supporting Information). The XPS results indicate that the interfacial Zr has been partially reduced<sup>[31,32]</sup> while La has been partially oxidized,<sup>[33,34]</sup> which further confirmed the formation of oxygen vacancies. Electron paramagnetic resonance (EPR) is also a common tool to probe the oxygen vacancy concentration in various materials.<sup>[35,36]</sup> The increasing peak intensity of oxygen vacancies modified LLZTO (named as OV-LLZTO) compared with pristine LLZTO (**Figure 1c**) clearly indicates the successful introduction of oxygen vacancies, which is consistent with the color change (**Figure S4**, Supporting Information) since electrons trapped in oxygen vacancies tend to be excited by light.<sup>[37,38]</sup> More oxygen vacancies will be introduced in LLZTO particles

under elevated heating temperature (450 °C) with a darker color as shown in **Figure S4** (Supporting Information). In addition, no phase transition (XRD pattern in **Figure S5**, Supporting Information) can be observed for OV-LLZTO after above treatment.

Next, different mass ratios of OV-LLZTO are added to the PEO/LiTFSI-based electrolytes and CSE membranes with an average thickness of 60  $\mu\text{m}$  can be obtained (**Figure S6**, Supporting Information). Based on the ionic conductivity (**Figure S7**, Supporting Information), it can be learned that the optimum ratio of OV-LLZTO is 10 wt.%, which is consistent with previously reported garnet-type ISE fillers.<sup>[39,40,41]</sup> Therefore, 10 wt.% is adopted for the preparation of CSEs containing LLZTO (LLZTO/PEO) and OV-LLZTO (OV-LLZTO/PEO). Different surface micromorphology of the two CSEs can be captured by SEM images (**Figure S8**, Supporting Information), LLZTO/PEO membrane has a blocky and flat surface, whereas OV-LLZTO/PEO shows an intertwined surface. Arrhenius plots of different solid electrolytes (**Figure 1d**; see detailed values in **Table S1** and the corresponding Nyquist plots in **Figure S9**, Supporting Information) show that a more significant boosting effect on the overall ionic conductivity of PEO is demonstrated by OV-LLZTO ( $5.6 \times 10^{-4} \text{ S cm}^{-1}$  at 60 °C) compared to that of LLZTO ( $3.7 \times 10^{-4} \text{ S cm}^{-1}$  at 60 °C). The lowered melting point of OV-LLZTO/PEO (56.3 °C) and LLZTO/PEO (57.5 °C) measured by differential scanning calorimetry (DSC) indicates promoted mobility of PEO segments is enabled by both fillers (**Figure 1e**). Linear sweep voltammetry curves of different electrolytes indicate OV-LLZTO/PEO shows an increased electrochemical upper voltage window of  $\approx 4.3 \text{ V}$  (**Figure S10**, Supporting Information), outweighing that of LLZTO/PEO and PEO ( $\approx 4$  and 4.2 V respectively). Interestingly, atomic force microscope (AFM) images demonstrate markedly different interfacial micromorphology for these solid electrolytes (**Figure S11**, Supporting Information). Agglomerated and blocky domains can be observed on filler-free PEO, corresponding to its high crystallinity. The addition of LLZTO particles transforms the blocky PEO into flocculent state with a certain degree of orientation, which confirms the decrease of crystallinity. By sharp contrast, after the introduction of oxygen vacancies, the flocculent surface becomes more disordered, where PEO segments become curly and intertwine with apparent undulation, which is consistent with SEM observation (**Figure S8**, Supporting Information). Such distinctive difference in the micromorphology is in good accordance with the DSC results: despite showing the same particle size and crystalline structure, OV-LLZTO has a stronger tendency to achieve the disordering of PEO domain than LLZTO. Moreover, a much-improved  $\text{Li}^+$  transference

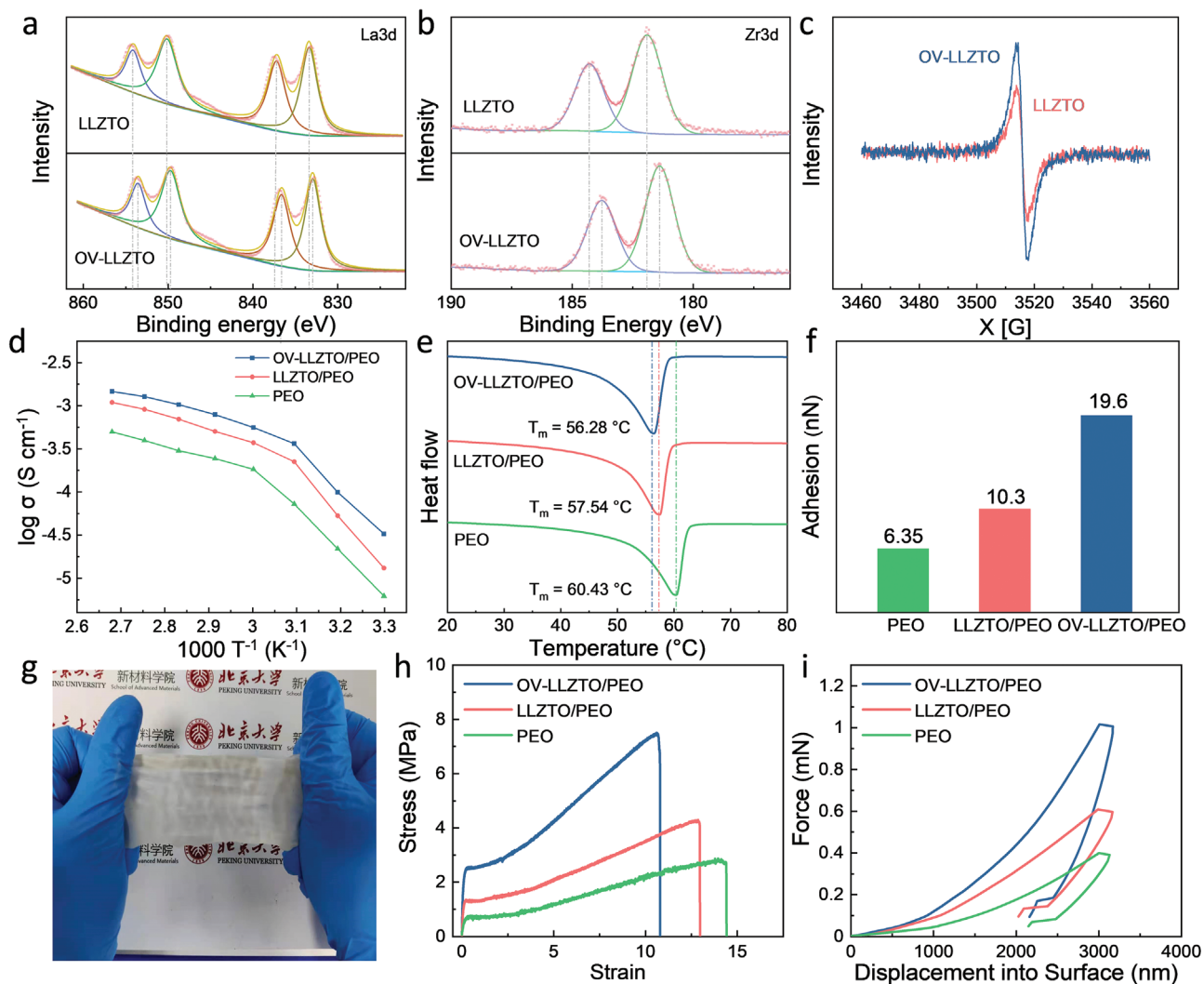


**Figure 1.** Characterizations of OV-LLZTO/PEO. a) La3d spectra and b) Zr3d spectra. c) EPR spectra of the pristine LLZTO and OV-LLZTO. d) Arrhenius plots of different electrolytes under different temperatures. e) DSC curves and the corresponding melting temperatures. f) The average interfacial adhesion force measured by AFM. g) Images of a sizable OV-LLZTO/PEO membrane being stretched. h) Stress–strain curves and i) nano-indentation curves of different membranes.

number ( $t_{Li^+}$ ) of 0.328 (Figure S12, Supporting Information) can be measured for OV-LLZTO/PEO (see detailed data in Figure S13, Supporting Information). This tendency well agrees with previous reports where oxygen vacancies are found to trap anions and facilitate the disassociation of Li-salts in PEO.<sup>[42,43]</sup>

In addition to ion conductivity, the interfacial contact between solid electrolyte and both electrodes determine the rate capability of solid batteries.<sup>[20,44]</sup> Herein, interfacial adhesion forces of electrolyte membranes are measured by AFM (the distribution mappings are shown in Figure S14, Supporting Information). The comparison of average adhesion forces of different electrolytes (Figure 1f) clearly shows that OV-LLZTO/PEO exhibits the highest value (19.6 nN) compared to PEO (6.4 nN) and LLZTO/PEO (10.1 nN), suggesting the best interfacial wetting ability with both electrodes. The high adhesion force could be attributed to the interfacial flocculent state of PEO, which potentially possesses a higher effective surface area to facilitate better interfacial contact.

Mechanical properties are crucial for the safe application and large-scale production of solid electrolytes in addition to ionic conductivity. Figure 1g demonstrates that sizable OV-LLZTO/PEO membranes with good stretching ability can be synthesized, demonstrating its potential for scalable cell manufacture. Figure 1h shows the strain–stress curves of the three electrolyte membranes and Table S2 (Supporting Information) summarizes the maximum tensile strength and tensile modulus calculated from the stress–strain curves. LLZTO/PEO exhibits a larger maximum tensile strength (4.25 MPa) than the filler-free PEO membrane (2.79 MPa), which can be attributed to that LLZTO particles serves as mechanical buffer to dissipate the stress.<sup>[2,40]</sup> The maximum tensile strength of the OV-LLZTO/PEO can be further enhanced to 7.51 MPa, which is  $\approx 3$  times larger than the LLZTO/PEO. The improvement of maximum tensile strength promises operational reliability for scalable cell manufacturing and tolerance for abusive working conditions.<sup>[2,45,46]</sup> Nanoindentation measurements (Figure 1i) are

further conducted to analyze the compressive modulus of different membranes which simulates their capability to resist Li dendrite.<sup>[2,7,11,17]</sup> Similarly, OV-LLZTO/PEO presents the highest compressive modulus (20.21 MPa) compared with LLZTO/PEO (6.50 MPa) and filler-free PEO (2.95 MPa strength), indicating higher resistance toward Li dendrite growth.

## 2.2. O-Bridged Interface between OV-LLZTO and PEO

So far, ionic conductivity, surface adhesion force and mechanical strength are shown to be improved by the introduction

of oxygen vacancies. To reveal to the origin of these improved properties, computational simulation is conducted to evaluate the molecular interaction between the PEO chains and the different filler surface. The binding energy between PEO chains and different  $\text{Li}_7\text{La}_3\text{Zr}_2\text{O}_{12}$  (for convenience, Ta is neglected in the simulation due to its low content) surfaces is calculated (Figure 2a; Figure S15, Supporting Information). As presented by the inset in Figure 2a, oxygen vacancies on the surface of LLZTO provide anchoring points for the O atom of PEO chains, building an O-bridged interface between PEO and OV-LLZTO. As a result, oxygen vacancies on the surface effectively strengthen the binding energy (from 1.34 to 1.97 eV),

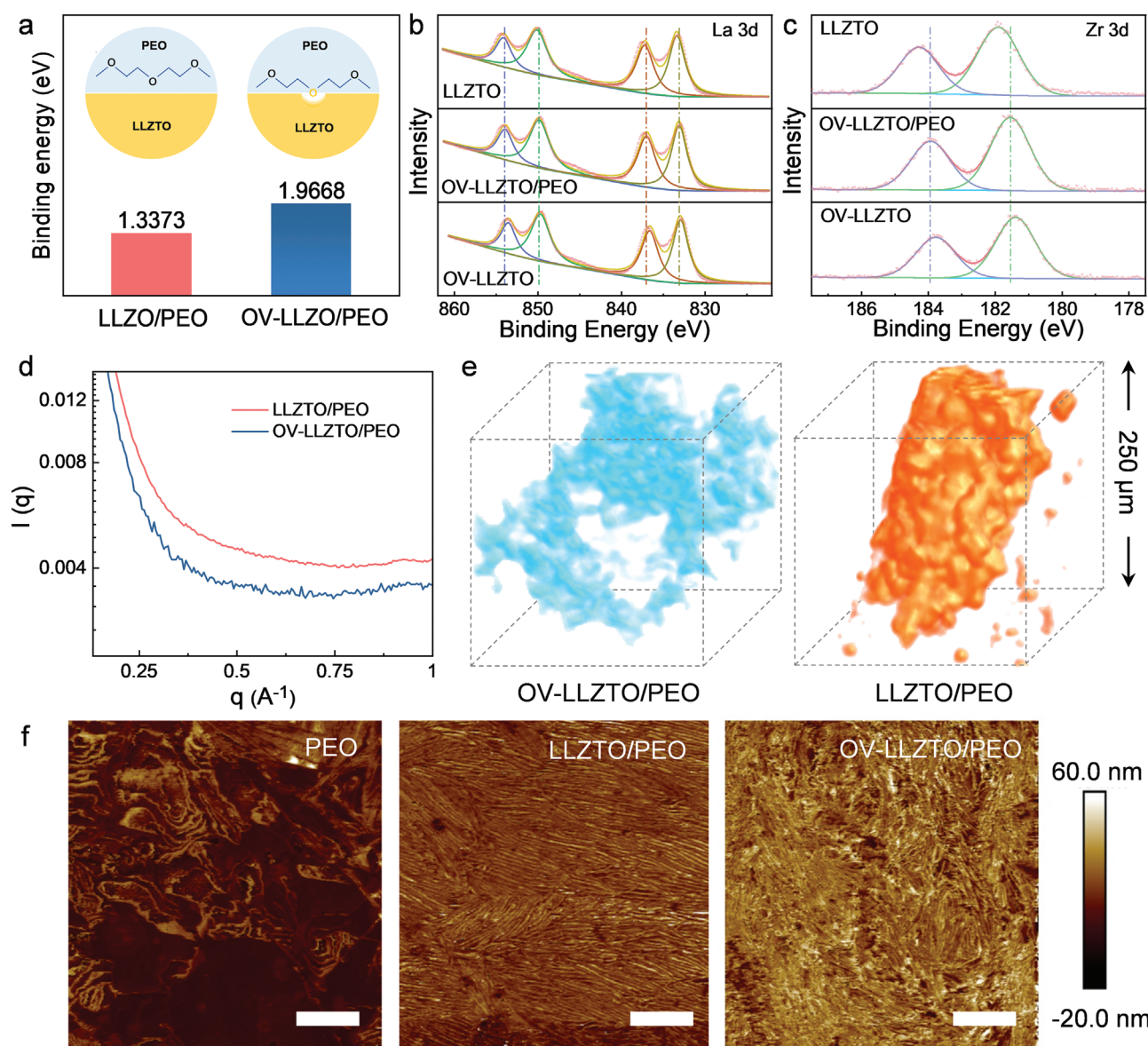


**Figure 2.** Improved mechanical properties enabled by oxygen vacancies. a) Simulated binding energy between different fillers and PEO. XPS analysis of solid electrolyte membranes: b) La3d spectra and c) Zr3d spectra. For better signal-noise ratios, the weight content of OV-LLZTO in the membrane is 50 wt.%. d) SAXS profiles of solid electrolyte membranes with a filler content of 50 wt.%. e) 3D structures of solid electrolyte membranes with 50 wt.% of fillers from X-ray micro-computed tomography, where the blank, blue and orange regions represent PEO, OV-LLZTO and LLZTO respectively. f) AFM deformation images of different solid electrolytes (scale bar = 2  $\mu\text{m}$ ).

suggesting a much stronger binding interaction between PEO and OV-LLZTO. This interaction is confirmed by XPS results (Figure 2b,c), where the peak shifts in binding energies for both Zr and La caused by oxygen vacancies are reduced after mixing with PEO (detailed peak positions are listed in Table S3, Supporting Information). Based on the changed chemical environment of interfacial Zr and La atoms, it can be inferred that oxygen atoms in PEO segments are anchored onto oxygen vacancies on the surface of LLZTO, forming strong binding sites via the “shared” oxygen atoms at the interface (demonstrated in Scheme 1). Such O-bridged interaction is also reflected by the degree of phase separation between PEO and LLZTO obtained from SAXS results (Figure 2d). The lower scattering intensity of OV-LLZTO/PEO than LLZTO/PEO indicates more uniform distribution and relieved phase separation due to the strong interaction of PEO and OV-LLZTO. Moreover, direct evidences are provided by 3D micro-structures of solid electrolyte membranes from visualized micro-computed tomography (micro-CT) scanning (Figure 2e). As for LLZTO/PEO, inevitable particle agglomeration occurs caused by huge surface energy of nano-sized particles, which not only compromises the overall mechanical strength but hinders Li-ion transportation in PEO matrix. On the contrary, the agglomeration of OV-LLZTO fillers is effectively prevented by PEO polymer segment firmly tight to their high-energy surface, thus more uniform distribution in PEO matrix. Combined with detailed morphologic characteristics of different membranes observed from AFM deformation images (Figure 2f), the enhancing mechanism for OV-LLZTO/PEO is proposed (Figure S16, Supporting Information): the addition of nano-sized LLZTO into PEO could effectively disrupt the crystalline domain of PEO,<sup>[40,47,48]</sup> enhancing the free movement of PEO segments. However, due to the relatively weak van der Waals’ force between LLZTO and PEO, the enhancing effect is not significant (as indicated by the oriented PEO morphology for LLZTO/PEO in Figure 2d). By sharp contrast, owing to the anchoring effect between OV-LLZTO and PEO via shared O atoms, the tensile and compressive strength of solid electrolyte membranes exhibit significant improvement. Furthermore, consistent with the surface morphology change shown in Figure S8 (Supporting Information), the strong molecular interaction leads to a flocculent morphology of the membrane, which is not only indicative of even lowered crystallinity, but also beneficial for homogeneous (soft) contact with electrodes.

### 2.3. Electrochemical Performance

As an important parameter to evaluate the stability toward Li dendrite growth, the maximum current density is tested for different electrolyte membranes by performing galvanostatic cycling for Li-Li symmetric cells with an increasing current density (Figure 3a). It is shown that the stable cycling with low polarization for OV-LLZTO/PEO is achieved with a current density as high as 0.7 mA cm<sup>-2</sup>, much higher than PEO (0.3 mA cm<sup>-2</sup>), and LLZTO/PEO (0.4 mA cm<sup>-2</sup>). The voltage profiles (Figure 3b) during long-term Li plating/stripping process are recorded at 60 °C with a current density of 0.2 mA cm<sup>-2</sup>. The cell using PEO failed after 68 h due to internal short circuit

while the addition of LLZTO in PEO managed to extend the lifespan to 332 h. By contrast, OV-LLZTO/PEO facilitates stable cycling of the Li-Li symmetric cell up to 1000 h with a lower voltage polarization (<0.043 V) compared to PEO and LLZTO/PEO. Furthermore, satisfactory cycling stability of OV-LLZTO/PEO under a high current density of 0.4 mA cm<sup>-2</sup> (Figure S17, Supporting Information) further demonstrates the great interface compatibility between OV-LLZTO/PEO and Li metal as well as enhanced lithium dendrite resistance. The lithium-ion mobility within the electrolyte and across the electrode/electrolyte interface has been improved by polymer-ceramic interfacial anchoring. First, the enhanced binding interaction between PEO and OV-LLZTO contributed to the reconstruction of PEO domains with decreased crystallinity. Second, the surface oxygen vacancies help to dissociate more free lithium-ions from the constraints of anions and ether units leading to a higher Li<sup>+</sup>-transference number.<sup>[49]</sup> Third, the flocculent surface morphology created homogeneous contact between electrolytes and electrodes, leading to a reduced charge transfer resistance ( $R_{ct}$ ) during cycling (Figure 3c; Figure S18, Supporting Information). The interfacial anchoring further promotes the mechanical strength of solid electrolyte membranes by strengthening intermolecular interaction, which not only mitigates lithium dendrite growth under higher operating current density, but also maintains the structural integrity of the electrolyte during long cycling (Figure S19, Supporting Information). As the result shows, undesirable cracks and pores can be observed on the cycled LLZTO/PEO surface, resulting in loss of contact and increased interfacial resistance. By contrast, the smooth surface is well-preserved for OV-LLZTO/PEO, which enables stable and fast lithium-ion diffusion.

Solid-state LiFePO<sub>4</sub> (LFP)||Li full cells were assembled and tested under 60 °C to evaluate the electrochemical performance of OV-LLZTO/PEO. Benefiting from the improved Li<sup>+</sup> conductivity and interfacial contact, the cell containing OV-LLZTO outperform others (Figure 3d), especially under high C-rates (128, 123, 115, and 109 mAh g<sup>-1</sup> under 5, 6, 7, and 8 C respectively). From the corresponding voltage curves (Figure 3e), the cell with OV-LLZTO/PEO electrolyte shows much-reduced overpotentials (Figure S20, Supporting Information). This result is in good accordance with the impedance spectra of the full-cells (Figure S21, Supporting Information), where OV-LLZTO/PEO also enables a lowest interfacial impedance. Furthermore, long-term cycling under 5 C is also tested and shown in Figure 3f. With an initial discharge capacity of 128 mAh g<sup>-1</sup>, much lowered overpotentials (Figures S22 and S23, Supporting Information) and a high-capacity retention of 84.2% after 1000 cycles, OV-LLZTO/PEO also delivers a superior cycling performance over others. The voltage degradation for both LLZTO/PEO and PEO is confirmed by the increasing interfacial resistance with cycling (Figure S24, Supporting Information), which originates from the unstable interface with Li metal anode under a relatively high current density (as demonstrated in Figure 3a). To further confirm the improvement of the electrochemical performance by O-bridged interaction, cycling performance of all-solid-state LFP batteries using LLZTO fillers with different concentrations of oxygen vacancies are tested under the current density of 5 C. All-solid-state LFP batteries using FOV-LLZTO/PEO with fewer oxygen vacancies exhibited a lower initial discharge capacity of

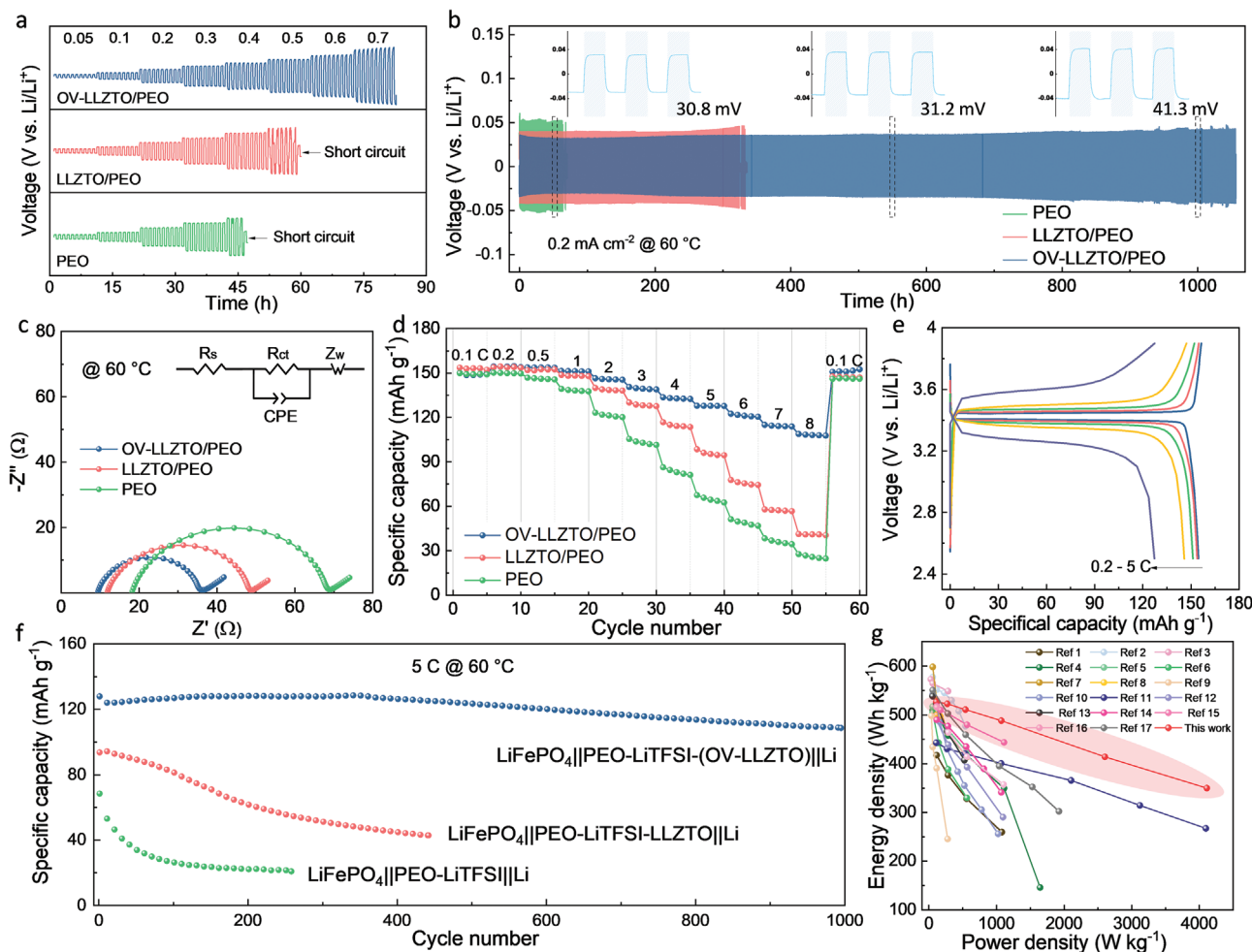


**Figure 3.** Improved electrochemical performance. a) Stepped current density galvanostatic cycling under different current density, b) galvanostatic cycling curves under  $0.2 \text{ mA cm}^{-2}$ , and c) EIS of Li–Li symmetric cells using different solid electrolytes. d) Rate performance of all-solid-state LFP batteries using different electrolytes and e) corresponding voltage curves of the cell using OV-LLZTO/PEO under different C-rates. f) Cycling performance of all-solid-state LFP batteries using different electrolytes under 5 C. All batteries are tested under  $60 \text{ }^\circ\text{C}$ . g) Comparison of the energy and power density with previously reported literatures. The corresponding literatures are listed in Table S4 (Supporting Information).

$116.4 \text{ mAh g}^{-1}$  and fast decay to  $91.4 \text{ mAh g}^{-1}$  after 400 cycles compared with the OV-LLZTO/PEO (Figure S25, Supporting Information). Benefiting from the improved lithium-ion mobility, OV-LLZTO/PEO also represents a superior cycling performance at  $30 \text{ }^\circ\text{C}$ , with a high initial discharge capacity of  $167.4 \text{ mAh g}^{-1}$  and high-capacity retention of 99.3% after 100 cycles (Figure S26, Supporting Information). By comparing the energy and power density delivered by LFP||OV-LLZTO/PEO||Li cells with those previously reported PEO-based all-solid-state LFP batteries (Figure 3g; see details listed in Table S4, Supporting Information), this work exhibits a state-of-the-art rate capability. In order to pursue higher energy density, as-developed CSEs are tentatively matched with  $\text{LiNi}_{0.83}\text{Co}_{0.11}\text{Mn}_{0.06}\text{O}_2$  (NCM) cathode to evaluate the electrochemical performance at high-voltage. Compared with LLZTO/PEO and PEO, OV-LLZTO/PEO achieves superior rate performance, with a high discharge capacity of 130.8 and  $125.8 \text{ mAh g}^{-1}$  under 4 and 5 C (Figure S27, Supporting Information). Such improvement in rate capability can also be seen from the lower voltage

polarization for OV-LLZTO/PEO in CV curves (Figure S28, Supporting Information). Moreover, OV-LLZTO/PEO exhibits the highest initial capacity of  $150.1 \text{ mAh g}^{-1}$  at 2 C as well as the minimum capacity decay after 150 cycles (Figure S29, Supporting Information). From the corresponding voltage curves (Figure S30, Supporting Information), OV-LLZTO/PEO shows much alleviated voltage polarization and ameliorated capacity retention, which is attributed to improved electrochemical stability (Figure S10, Supporting Information) and improved interfacial contact mentioned above.

To further demonstrate the potential of OV-LLZTO/PEO for practical application, all-solid-state LFP pouch cells are assembled and tested. The as-prepared pouch cells possess excellent flexibility that can be bent and winded around human arms while powering the light-emitting diode (LED) array as shown in Figure 4a. Similar to coin cells, the LFP pouch cell using OV-LLZTO/PEO also achieved excellent rate performance (Figure 4b) with low polarization (voltage curves in Figure 4c). The cycle performance results (Figure 4d) reveal that LFP pouch

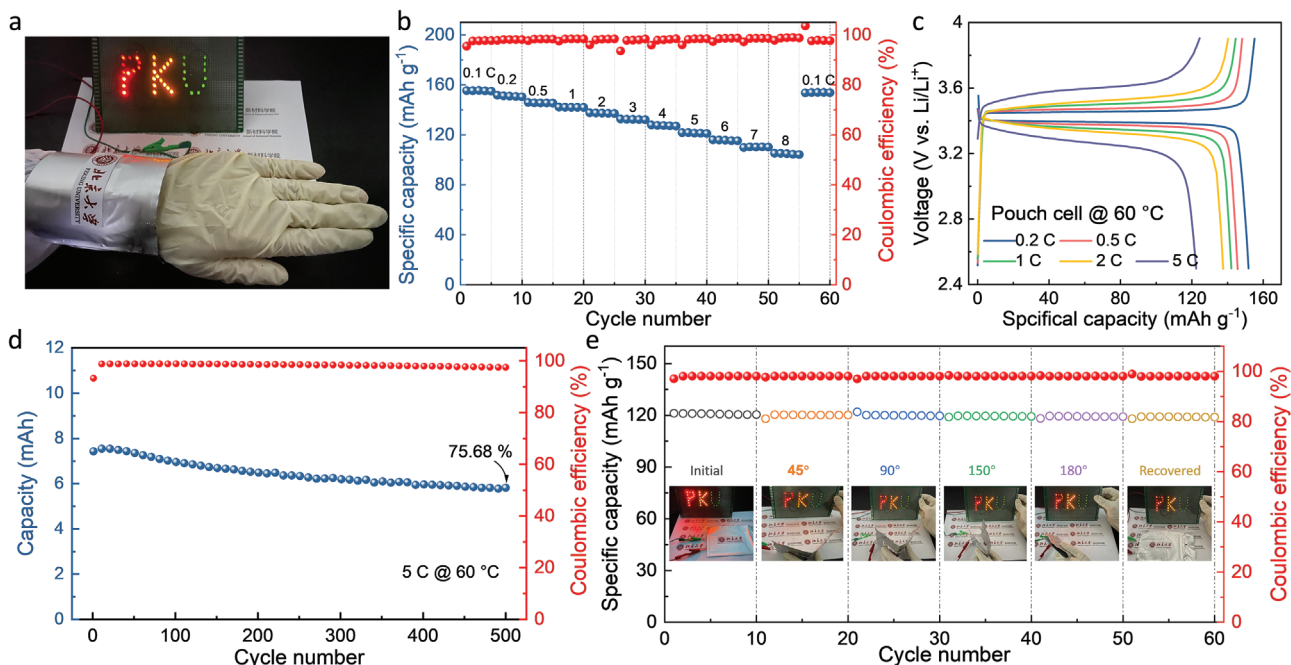


**Figure 4.** Solid-state pouch cell performance. a) Photograph of the flexible pouch cells. b) Rate performance under different C-rates and c) the corresponding voltage curves. d) Cycling performance under 5 C. e) Demonstration of foldability of the pouch cell (inset photos) and the cycling performance when bent to different angles. All galvanostatic cycling tests are carried out at 60 °C and photos are taken at room temperature.

cells can be stably cycled under 5 C with high-capacity retention (75.68% after 500 cycles). Owing to the excellent mechanical strength of OV-LLZTO/PEO, the LFP pouch cell work perfectly under different bending angles (Figure 4e) at 5 C. Moreover, even under extreme destructive conditions (such as cutting) at room temperature (Figure S31, Supporting Information), the pouch cell can still power the LED array without internal short circuit, which showcases the safety and reliability of OV-LLZTO/PEO in all-solid-state pouch cells. The tests involving human participants are approved by the Internal Review Board of Peking University Shenzhen Graduate School and the study conforms to recognized standards, such as the Declaration of Helsinki. Informed written consent was acquired from the participants for the studies.

### 3. Conclusions

In conclusion, through modifying LLZTO with surface defects and further compositing with PEO, a flexible composite solid electrolyte (OV-LLZTO/PEO) is designed and prepared for all-solid-state lithium metal batteries. The as-prepared OV-LLZTO/PEO shows improved ionic conductivity of  $5.6 \times 10^{-4} \text{ S cm}^{-1}$  at 60 °C, and more importantly, excellent tensile modulus (7.51 MPa), compressive modulus (20.21 MPa), elevated electrochemical window and enhanced interfacial compatibility to electrodes are exhibited owing to the unique anchoring effect of PEO chains on oxygen vacancies. Consequently, OV-LLZTO/PEO exhibits excellent stability with Li anode even under high working current density ( $0.7 \text{ mA cm}^{-2}$ ). Owing to the enhanced interfacial charge transfer and mechanical strength of OV-LLZTO/PEO, excellent cycling stability toward Li metal anode

is obtained, especially at higher current densities. More importantly, coupled with LFP cathode, all-solid-state full-cells deliver leading rate performance and power density among reported works. Flexible LFP pouch cells employing OV-LLZTO/PEO deliver excellent rate performance and capacity retention. By incorporating OV-LLZTO/PEO into a flexible pouch cell, excellent rate performance, cycling stability and safety features can be also obtained. Through demonstrating a microscopic strategy to manipulate the interaction between PEO and active fillers, this work points out a new direction to optimizing the performance of all-solid-state batteries.

### 4. Experimental Section

**Synthesis of LLZTO with Oxygen Vacancy:** Nano-sized LLZTO particles with the average diameter of 300 nm was directly purchased from MTI. Then the pristine LLZTO particles were sintered in the tube furnace at different temperatures (400 °C for FOV-LLZTO and 450 °C for OV-LLZTO) under the Ar/H<sub>2</sub> atmosphere for 10 h to introduce various concentrations of oxygen vacancies. The treated LLZTO was then transferred to Ar-filled glovebox for use.

**Preparation of Solid Electrolytes:** 0.144 g LiTFSI (Aladdin), 0.54 g PEO (Aldrich, Mw = 600000) and different amount of fillers were mixed in 12 mL anhydrous acetonitrile (Aladdin, 99%) and mechanically stirred for 12 h at 70 °C in the argon-filled glove-box to get a homogeneous solution. And then the solution was casted with doctor blade on the polytetrafluoroethylene (PTFE) plate and dried at 80 °C for 12 h in the glove-box.

**Materials Characterizations:** The X-Ray Diffraction (XRD) was performed on the Bruker D8 Advance powder X-ray diffractometer with  $2\theta$  in the range of 10–60° with a count time of 0.1 s per step to investigate the crystal structure of LLZTO. Electron paramagnetic resonance (EPR, Briker A300-10/12) was applied to measure the oxygen vacancies in different LLZTO solid electrolytes. X-ray photoelectron spectroscopy

(XPS, ESCALab2201-XL) was used to analyze the valence state evolution of the LLZTO particles. The stress and strain curves were measured by Force Gauge Model M7-2 at a stretching speed of 10 mm min<sup>-1</sup> at room temperature. Nano-indentation tests were carried out on U9820A Nano Indenter G200. Differential scanning calorimeter (DSC) tests were conducted on the Mettler Toledo in the temperature range from room temperature to 80 °C at a heating rate of 10 min<sup>-1</sup> under N<sub>2</sub> atmosphere. Raman tests were conducted on the Xplora plus Raman spectrometer (HORIBA) with the excitation wavelength of 785 nm. The Raman spectrometer was calibrated using the standard silicon wafer sample. The nano-scale morphology and surface adhesion forces were measured by Bruker multimode 8 atomic force microscope. Scanning electron microscope (SEM) was taken by Zeiss SUPRA55. SAXS measurements were performed at an X-ray scattering instrument (Xeuss 3.0) with an accessible  $q$  range from 0.07 to 2.3 nm<sup>-1</sup>. X-ray micro-computed tomography was performed by Bruker SkyScan1172. In order to clearly distinguish the distribution of each component, the thickness of solid electrolyte membranes made for micro-CT was controlled at ≈500 μm by casting method. The images were acquired at a final resolution of 1.2 μm at 80 kV accelerating voltage and 100 μA current.

**Electrochemical Testing:** Coin-cells were assembled in the argon-filled glove-box. CV measurements were carried out with a model CHI660C electrochemical workstation (CHI, Shanghai) under a scan rate of 0.1 mV s<sup>-1</sup> at 60 °C. The ionic conductivity was evaluated by electrochemical impedance spectroscopy (EIS) in the frequency range from 1 MHz to 0.1 Hz between 30 to 100 °C using an electrochemical workstation (Solartron 1470E). The electrolytes were sandwiched by two pieces of stainless-steel disks. The ionic conductivities ( $\delta$ ) were calculated by the following equation:

$$\delta = \frac{L}{SR_b} \quad (1)$$

where  $S$  is the area of the contacting surface of the stainless-steel disk with the membranes,  $L$  is the thickness of the membranes and  $R_b$  is the bulk resistance of the membranes.

The stability against Li anode was evaluated by galvanostatic cycling of Li-Li symmetric cells under various current densities using a Neware battery testing system at 60 °C.

The lithium transference numbers were measured by chronoamperometry and AC impedance spectra using lithium symmetric batteries. The EIS spectra before and after the 10 mV potential being applied are obtained. The values were calculated according to the following equation:

$$t^+ = \frac{I_{SS}(\Delta V - I_0 R_0)}{I_0(\Delta V - I_{SS} R_{SS})} \quad (2)$$

where  $I_0$  and  $I_{SS}$  are the initial and steady state current,  $\Delta V$  is the polarization potential at 10 mV, and  $R_0$  and  $R_{SS}$  are the initial and steady state resistance.

The all-solid-state full-batteries were tested applying LiFePO<sub>4</sub> (LFP) / LiNi<sub>0.83</sub>Co<sub>0.11</sub>Mn<sub>0.06</sub>O<sub>2</sub> (NCM) and cathode materials. The LFP / (NCM) electrodes were prepared by mixing the LFP, acetylene black and PVDF with the mass ratio is 8:1:1 in NMP solvent followed by 10 h stirring to get homogenous solution. The mixture solution was then coated on an Al foil and dried in the vacuum oven overnight at 80 °C. The mass loading of the LFP / NCM electrodes was ≈2 mg cm<sup>-2</sup>. Lithium pellets were used as anodes. The batteries were cycled between 2.5–3.9 V for LFP cells and 2.7–4.3 V (vs Li/Li<sup>+</sup>) for NCM cells at 60 °C using a Neware battery testing system. For pouch-cells, the cathode was prepared by mixing LFP, acetylene black, PEO and LiTFSI in anhydrous acetonitrile with the mass ratio was 50:30:20:2 for 10 h. Then the past was coated on an Al foil and dried for 12 h at 80 °C. The mass loading of LiFePO<sub>4</sub> was ≈2 mg cm<sup>-2</sup>.

**Simulation Method:** The PEO polymer chain was optimized on the Gaussian09 package at B3LYP/6-311G\*\* level of theory. The plane wave

DFT implemented in the Vienna ab initio simulation package (VASP) with projector augmented wave (PAW) potentials to calculate the binding energy between PEO and Li<sub>6.4</sub>La<sub>3</sub>Zr<sub>1.4</sub>Ta<sub>0.6</sub>O<sub>12</sub>. The exchange-correlation interaction was treated with the generalized gradient approximation (GGA) of Perdew–Burke–Ernzerhof (PBE + U). The criterion for convergence was that the total energy difference is below 1.0 × 10<sup>-5</sup> eV per atom and the residual forces are below 0.01 eV Å<sup>-1</sup>. The cut-off energy was set to 520 eV in the structure optimization and the energy calculation. The surface structure was modeled by a supercell with a dimension of 13.17 Å × 13.17 Å × 16 Å that contained two Li<sub>6.4</sub>La<sub>3</sub>Zr<sub>1.4</sub>Ta<sub>0.6</sub>O<sub>12</sub> molecular units. It was used a (1 × 1 × 1)  $k$ -point grid determined by Monkhorst-Pack method to sample the Brillouin zone. The calculation binding energy of PEO to the Li<sub>6.4</sub>La<sub>3</sub>Zr<sub>1.4</sub>Ta<sub>0.6</sub>O<sub>12</sub> was defined as the following:  $\Delta E_{\text{bind}} = E(\text{PEO}/\text{base}) - E(\text{PEO}) - E(\text{base})$ .

## Supporting Information

Supporting Information is available from the Wiley Online Library or from the author.

## Acknowledgements

Y.F., K.Y., S.X. contributed equally to this work. This research was financially supported by National Key R&D Program of China (2016YFB07006000) and Shenzhen Science and Technology Research Grant (JCYJ20160531141048950).

## Conflict of Interest

The authors declare no conflict of interest.

## Data Availability Statement

Research data are not shared

## Keywords

interfacial binding, mechanical strength, rate performance, solid-state batteries, solid-state electrolytes

Received: September 18, 2022

Revised: December 2, 2022

Published online:

- [1] M. C. Pang, K. Yang, R. Brugge, T. Zhang, X. Liu, F. Pan, S. Yang, A. Aguadero, B. Wu, M. Marinescu, H. Wang, G. J. Offer, *Mater. Today* **2021**, *49*, 145.
- [2] L. Z. Fan, H. He, C. W. Nan, *Nat. Rev. Mater.* **2021**, *6*, 1003.
- [3] J. C. Bachman, S. Muy, A. Grimaud, H. H. Chang, N. Pour, S. F. Lux, O. Paschos, F. Maglia, S. Lupart, P. Lamp, L. Giordano, Y. Shao-Horn, *Chem. Rev.* **2016**, *116*, 140.
- [4] L. Xu, Y. Lu, C. Z. Zhao, H. Yuan, G. L. Zhu, L. P. Hou, Q. Zhang, J. Q. Huang, *Adv. Energy Mater.* **2021**, *11*, 2002360.
- [5] A. Banerjee, X. Wang, C. Fang, E. A. Wu, Y. S. Meng, *Chem. Rev.* **2020**, *120*, 6878.
- [6] H. Song, S. Xue, S. Chen, Z. Wang, Y. Song, J. Li, Z. Song, L. Yang, F. Pan, *Chin. J. Struct. Chem.* **2022**, *41*, 2205048.

- [7] R. Chen, Q. Li, X. Yu, L. Chen, H. Li, *Chem. Rev.* **2020**, *120*, 6820.
- [8] D. Cao, X. Sun, Q. Li, A. Natan, P. Xiang, H. Zhu, *Matter.* **2020**, *3*, 57.
- [9] J. Li, Y. Ji, H. Song, S. Chen, S. Ding, B. Zhang, L. Yang, Y. Song, F. Pan, *Nano-Micro Lett.* **2022**, *14*, 191.
- [10] Y. Zheng, Y. Yao, J. Ou, M. Li, D. Luo, H. Dou, Z. Li, K. Amine, A. Yu, Z. Chen, *Chem. Soc. Rev.* **2020**, *49*, 8790.
- [11] Z. Cheng, T. Liu, B. Zhao, F. Shen, H. Jin, X. Han, *Energy Storage Mater.* **2021**, *34*, 388.
- [12] G. Xi, M. Xiao, S. Wang, D. Han, Y. Li, Y. Meng, *Adv. Funct. Mater.* **2021**, *31*, 2007598.
- [13] Y. Ji, K. Yang, M. Liu, S. Chen, X. Liu, B. Yang, Z. Wang, W. Huang, Z. Song, S. Xue, Y. Fu, L. Yang, T. S. Miller, F. Pan, *Adv. Funct. Mater.* **2021**, *31*, 2104830.
- [14] Y. Tominaga, K. Yamazaki, *Chem* **2014**, *50*, 4448.
- [15] L. Chen, W. Li, L. Z. Fan, C. W. Nan, Q. Zhang, *Adv. Funct. Mater.* **2019**, *29*, 1901047.
- [16] M. Keller, A. Varzi, S. Passerini, *J. Power Sources* **2018**, *392*, 206.
- [17] S. Li, S. Q. Zhang, L. Shen, Q. Liu, J. bin Ma, W. Lv, Y. B. He, Q. H. Yang, *Adv. Sci.* **2020**, *7*, 1903088.
- [18] S. Tang, W. Guo, Y. Fu, *Adv. Energy Mater.* **2021**, *11*, 2000802.
- [19] Y. Liu, B. Xu, W. Zhang, L. Li, Y. Lin, C. Nan, *Small* **2020**, *16*, e1902813.
- [20] L. Yang, Z. Wang, Y. Feng, R. Tan, Y. Zuo, R. Gao, Y. Zhao, L. Han, Z. Wang, F. Pan, *Adv. Energy Mater.* **2017**, *7*, 1701437.
- [21] R. J. Chen, Y. B. Zhang, T. Liu, B. Q. Xu, Y. H. Lin, C. W. Nan, Y. Shen, *ACS Appl. Mater. Interfaces* **2017**, *9*, 9654.
- [22] L. Chen, Y. Li, S. P. Li, L. Z. Fan, C. W. Nan, J. B. Goodenough, *Nano Energy* **2018**, *46*, 176.
- [23] Z. Li, H. M. Huang, J. K. Zhu, J. F. Wu, H. Yang, L. Wei, X. Guo, *ACS Appl. Mater. Interfaces* **2019**, *11*, 784.
- [24] J. Zheng, M. Tang, Y. Y. Hu, *Angew. Chem., Int. Ed.* **2016**, *55*, 12538.
- [25] H. Zhai, P. Xu, M. Ning, Q. Cheng, J. Mandal, Y. Yang, *Nano Lett.* **2017**, *17*, 3182.
- [26] X. Wang, H. Zhai, B. Qie, Q. Cheng, A. Li, J. Borovilas, B. Xu, C. Shi, T. Jin, X. Liao, Y. Li, X. He, S. Du, Y. Fu, M. Dontigny, K. Zaghbi, Y. Yang, *Nano Energy* **2019**, *60*, 205.
- [27] J. Zheng, P. Wang, H. Liu, Y. Y. Hu, *ACS Appl. Energy Mater.* **2019**, *2*, 1452.
- [28] Y. Zhao, C. Wu, G. Peng, X. Chen, X. Yao, Y. Bai, F. Wu, S. Chen, X. Xu, *J. Power Sources* **2016**, *301*, 47.
- [29] X. Zhu, K. Wang, Y. Xu, G. Zhang, S. Li, C. Li, X. Zhang, X. Sun, X. Ge, Y. Ma, *Energy Storage Mater.* **2021**, *36*, 291.
- [30] J. Zheng, Y. Y. Hu, *ACS Appl. Mater. Interfaces* **2018**, *10*, 4113.
- [31] Y. Gao, S. Sun, X. Zhang, Y. Liu, J. Hu, Z. Huang, M. Gao, H. Pan, *Adv. Funct. Mater.* **2021**, *31*, 2009692.
- [32] M. Naguib, A. Sharafi, E. C. Self, H. M. Meyer, J. Sakamoto, J. Nanda, *ACS Appl. Mater. Interfaces* **2019**, *11*, 42042.
- [33] H. Zhang, S. Hao, J. Lin, *J. Alloy. Compd.* **2017**, *704*, 109.
- [34] M. Zarabian, M. Bartolini, P. Pereira-Almao, V. Thangadurai, *J. Electrochem. Soc.* **2017**, *164*, A1133.
- [35] Z. Li, Y. Ren, L. Mo, C. Liu, K. Hsu, Y. Ding, X. Zhang, X. Li, L. Hu, D. Ji, G. Cao, *ACS Nano* **2020**, *14*, 5581.
- [36] Y. Shi, D. Zhang, C. Chang, K. Huang, R. Holze, *J. Alloy. Compd.* **2015**, *639*, 274.
- [37] T. v. Perevalov, O. E. Tereshenko, V. A. Gritsenko, V. A. Pustovarov, A. P. Yelisseyev, C. Park, J. H. Han, C. Lee, *J. Appl. Phys.* **2010**, *108*, 013501.
- [38] D. Liu, S. J. Clark, J. Robertson, *Appl. Phys. Lett.* **2010**, *108*, 013501.
- [39] T. A. Zegeye, W. N. Su, F. W. Fenta, T. S. Zeleke, S. K. Jiang, B. J. Hwang, *ACS Appl. Energy Mater.* **2020**, *3*, 11713.
- [40] H. Zhuang, W. Ma, J. Xie, X. Liu, B. Li, Y. Jiang, S. Huang, Z. Chen, B. Zhao, *J. Alloy. Compd.* **2021**, *860*, 157915.
- [41] A. S. Best, J. Adebahr, P. Jacobsson, D. R. MacFarlane, M. Forsyth, *Macromolecules* **2001**, *34*, 4549.
- [42] W. Liu, N. Liu, J. Sun, P. C. Hsu, Y. Li, H. W. Lee, Y. Cui, *Nano Lett.* **2015**, *15*, 2740.
- [43] H. Chen, D. Adekoya, L. Hencz, J. Ma, S. Chen, C. Yan, H. Zhao, G. Cui, S. Zhang, *Adv. Energy Mater.* **2020**, *10*, 2000049.
- [44] Z. Wang, L. Yang, J. Liu, Y. Song, Q. Zhao, K. Yang, F. Pan, *ACS Appl. Mater. Interfaces* **2020**, *12*, 48677.
- [45] J. Zhang, N. Zhao, M. Zhang, Y. Li, P. K. Chu, X. Guo, Z. Di, X. Wang, H. Li, *Nano Energy* **2016**, *28*, 447.
- [46] J. Wen, Q. Zhao, X. Jiang, G. Ji, R. Wang, G. Lu, J. Long, N. Hu, C. Xu, *ACS Appl. Mater. Interfaces* **2021**, *4*, 3660.
- [47] Y. Huang, Z. Zhang, H. Gao, J. Huang, C. Li, *Solid State Ionics* **2020**, *356*, 115437.
- [48] C. Bai, Z. Wu, W. Xiang, G. Wang, Y. Liu, Y. Zhong, B. Chen, R. Liu, F. He, X. Guo, *J. Power Sources* **2020**, *472*, 228461.
- [49] Y. Song, L. Yang, J. Li, M. Zhang, Y. Wang, S. Li, S. Chen, K. Yang, K. Xu, F. Pan, *Small* **2021**, *17*, 2102039.